RSC Sustainability

ROYAL SOCIETY OF CHEMISTRY

PAPER

View Article Online
View Journal | View Issue

Cite this: *RSC Sustainability*, 2026, **4**, 1544

Microwave assisted construction of a SnO_x/$ZnSn(OH)_6$ heterojunction for photocatalytic CO_2 cycloaddition

Soumita Sarkar, Soumalya Banerjee, Sk Afsar Ali, Sunny Sarkar and Astam K. Patra *

The utilization of photochemical reactions to convert CO_2 and epoxides into valuable cyclic organic carbonates is a highly sought-after process in various industries. The development of a high-performance photocatalyst for this cycloaddition of CO_2 presents a significant challenge, particularly in the context of sustainability initiatives. To effectively harness light energy for CO_2 value-added processes, we have engineered a SnO_x-decorated perovskite-type $ZnSn(OH)_6$ photocatalyst. Through analysis using UV-Vis and Mott–Schottky plots, we have gained insights into the electronic structure of the materials, including adsorption, band gap, and band position. The incorporation of SnO_x into the $ZnSn(OH)_6$ cube has significantly improved charge transfer, as demonstrated by photocurrent and Nyquist measurement. This molecular framework lays the foundation for the high photocatalytic performance and stability exhibited by SnO_x/$ZnSn(OH)_6$ in facilitating the cycloaddition of CO_2 and various epoxides to produce cyclic carbonates. The SnO_x/$ZnSn(OH)_6$ catalyst demonstrates high performance, achieving an impressive yield of ≈95% and reaction activity of 4750.0 μmol g^{-1} h^{-1} with high values of green chemistry metrics (AE = 100%, RME = 92.98%, PMI = 5.99 and *E* factor = 4.99). This performance surpasses that of several other catalysts. Further examination through LSV, EPR and electron–hole scavenger tests has provided a deeper understanding of the reaction mechanism under light irradiation. Additionally, the materials have demonstrated good stability, highlighting their potential in sustainable processes.

Received 9th October 2025
Accepted 1st February 2026

DOI: 10.1039/d5su00789e

rsc.li/rscsus

Sustainability spotlight

Most of the current processes for the transformation of CO_2 into value added chemicals have various limitations from an experimental point of view such as (i) requiring extreme temperature or pressure with a lengthy reaction time; (ii) use of hazardous catalysts; (iii) use of non-ecofriendly solvents. In this work, we have carried out the photocatalytic conversion of CO_2 and epoxides into valuable cyclic organic carbonates using the SnO_x/$ZnSn(OH)_6$ material at ambient temperature and pressure. The catalysts were synthesized using a commercial microwave reactor with a short reaction time of 2 min. The catalysts have a number of beneficial qualities like simpler separation and recyclability. Utilising light is a sustainable, affordable, adaptable, and energy-efficient process. The SnO_x/$ZnSn(OH)_6$ catalyst demonstrates exceptional performance, achieving an impressive yield of ≈95%, and a reaction activity of 4750.0 μmol g^{-1} h^{-1} for the photocatalytic cycloaddition of CO_2 using an eco-friendly solvent (PEG 600), SnO_x/$ZnSn(OH)_6$ and TBAB cocatalyst. Our synthesized catalyst also provides high values of green chemistry metrics (AE = 100%, RME = 92.98%, PMI = 5.99 and *E* factor = 4.99). Furthermore, the catalyst's reusability was assessed, showing that it maintained photocatalytic activity for up to six consecutive cycles, highlighting its potential for reuse.

1. Introduction

The transformation of carbon dioxide (CO_2) into valuable chemical products has attracted significant attention as a promising approach and crucial area of research, offering potential solutions to mitigate climate change and utilize this abundant carbon source.[1–3] One of the most promising pathways involves the photochemical reaction of CO_2 with epoxides, which shows great potential for the eco-friendly production of cyclic carbonates.[4,5] Photochemical CO_2 fixation presents a sustainable and energy-efficient substitute for conventional thermal or catalytic techniques, utilizing light as a driving force to activate CO_2.[6–10] The use of light for driving CO_2 conversion not only provides a mild reaction environment but also enables selective transformations that are difficult to achieve under conventional conditions.[11–14] The photocatalytic CO_2 cycloaddition process is highly sought after due to its 100% CO_2 utilization and significant economic benefits.[15] One example of its effectiveness is the conversion of styrene oxide to styrene carbonate by simply adding CO_2. The resulting cyclic organic carbonates are widely used as aprotic polar solvents,[16]

Department of Chemistry, University of Kalyani, Kalyani 741235, West Bengal, India. E-mail: astamchem18@klyuniv.ac.in

polycarbonate precursors,[17] and electrolytes for secondary batteries.[18] However, the challenge lies in the poor electron-withdrawing capacity and strong steric hindrance of the phenyl group in styrene oxide, making the cycloaddition of CO_2 difficult.[19] Developing effective catalysts for CO_2 fixation to high-value compounds is therefore a worthwhile but challenging endeavor. Various catalysts have been developed for the CO_2 cycloaddition process, such as semiconductors,[20–23] single-atom catalysts,[24,25] organocatalysts,[26,27] MOF-based catalysts,[28] semiconductor quantum dots,[29,30] and nanoclusters[31,32] which facilitate the activation of CO_2 and epoxide substrates under light irradiation. Studies have explored various strategies to optimize reaction conditions, such as the use of co-catalysts, solvent-free conditions, and solar-driven processes, to improve yields and selectivity.[33,34] Unfortunately, many of these catalysts require harsh conditions, leading to laborious post-reaction treatment, environmental issues, and increased energy consumption. As a result, there is a pressing need for the green and sustainable synthesis of CO_2 cycloaddition catalysts. Researchers are turning their attention to the photocatalytic CO_2 cycloaddition reaction with epoxides due to its sustainable process and environmentally friendly nature.[35]

Semiconductor heterojunctions play a crucial role in the advancement of new photocatalysts.[36–38] These heterojunctions are created at the interface between two materials with different semiconductor band gaps, usually composed of distinct semiconductor compounds.[36] The distinct properties found at these interfaces, including customized band alignments, effective charge carrier transport, and decreased recombination rates, allow for the development of high-performance materials. Through precise engineering of these interfaces, significant progress has been made in the fields of photovoltaics and photocatalysis.[39] The key to achieving optimal performance in semiconductor heterojunctions lies in the careful selection of materials, the precise control of interface quality, and the understanding of charge transfer mechanisms at the junction. With the development of new materials, such as perovskites and two-dimensional materials, and advancements in fabrication techniques, the scope of semiconductor heterojunctions continues to expand.[40–42] In particular, metal oxide/hydroxide heterojunction materials have shown promise in a wide range of applications due to their tunable electronic properties and efficient carrier dynamics.[43] Among the emerging material systems, the $SnO_x/ZnSn(OH)_6$ heterojunction has shown considerable promise because of its unique electronic properties, stability, and efficient charge separation capabilities.[44–46] SnO_x (tin oxide) is widely recognized for its high conductivity, optical transparency, and suitability as an electron transport material in solar cells and photocatalysts,[47,48] while $ZnSn(OH)_6$ offers a distinct advantage due to its mixed-valence structure and tunable band gap.[49] The combination of these two materials into a heterojunction structure can significantly enhance the performance of devices such as photocatalysts for water splitting, sensors, and field-effect transistors. Recently, Chen and his colleagues synthesized a small quantity of SnO_2-decorated $ZnSn(OH)_6$, which proved to be an extremely efficient photocatalyst for the decomposition of gaseous benzene.[44] Their study aimed to uncover the synergistic effect between SnO_2 and $ZnSn(OH)_6$.

In this study, we demonstrate the inclusion of SnO_x into $ZnSn(OH)_6$, resulting in the high conversion of CO_2 gas to organic carbonate. The presence of SnO_x on $ZnSn(OH)_6$ plays a crucial role in reducing charge recombination. The $SnO_x/ZnSn(OH)_6$ catalyst demonstrates high performance, achieving an impressive yield of ≈95% and a reaction activity of 4750.0 μmol g^{-1} h^{-1} with AQY 722.89 × 10^{-5}.

2. Results and discussion

2.1 Morphology, phase and structural analysis

Cuboid-shaped zinc hydroxystannate [$ZnSn(OH)_6$] was successfully synthesized using a microwave-assisted synthetic route without the need for a template. The synthetic process included zinc nitrate hexahydrate, tin(IV) chloride, sodium hydroxide, and deionized water. This innovative method facilitated the efficient production of zinc hydroxystannate cuboids in an aqueous solution, leading to a remarkably short reaction time of just 2 minutes. Furthermore, the SnO_x-decorated zinc hydroxystannate [$SnO_x/ZnSn(OH)_6$] was synthesized by utilizing zinc hydroxystannate cubes and tin(IV) chloride through a microwave-assisted synthetic route. The specific procedures for these reactions are outlined in Scheme 1 and the Experimental section.

Fig. 1a, b and c, d shows the SEM pictures of $ZnSn(OH)_6$ and $SnO_x/ZnSn(OH)_6$ materials respectively. Fig. 1a and b displays a SEM image of cuboid-shaped materials ranging in size from 0.5 to 1.7 μm in length, 0.5 to 1.6 μm in width, and 0.4 to 1.4 μm in height. The surface morphology of materials remains consistent across the entire product. But the $SnO_x/ZnSn(OH)_6$ material shows a cuboid shape with small-size nanoparticles on the surfaces. Furthermore, the SnO_x particles on the surface of the $ZnSn(OH)_6$ cuboid are examined through high-resolution transmission electron microscopy (TEM) analysis, as depicted in Fig. 2. The powder XRD features obtained from $ZnSn(OH)_6$

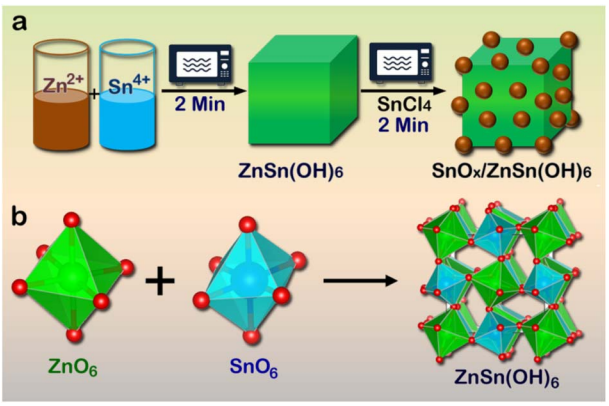

Scheme 1 (a) The microwave synthetic route had been used to produce cuboid shaped zinc hydroxystannate [$ZnSn(OH)_6$] and SnO_x decorated $ZnSn(OH)_6$ materials. (b) The crystal structure of $ZnSn(OH)_6$ showing ZnO_6 octahedra corner (green) and SnO_6 octahedra (light blue) and the unit cell of [$ZnSn(OH)_6$].

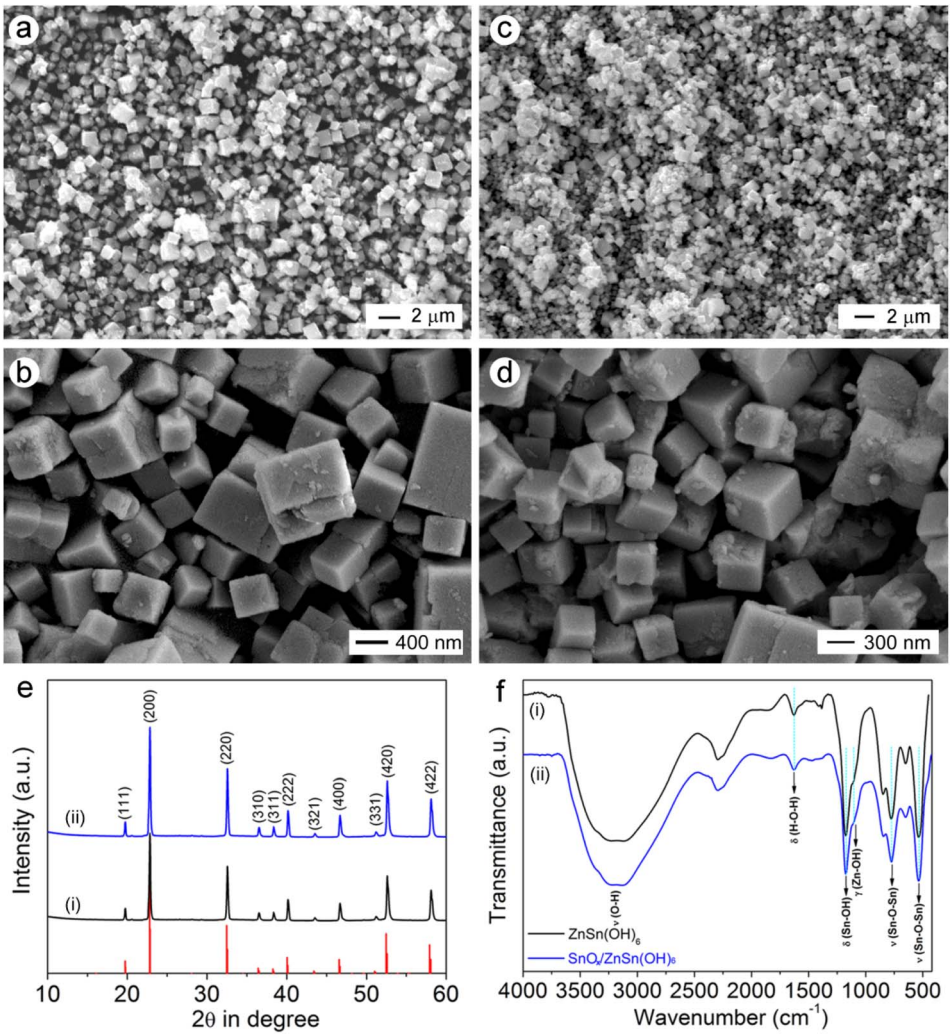

Fig. 1 Low and high magnification SEM images of (a and b) $ZnSn(OH)_6$ and (c and d) $SnO_x/ZnSn(OH)_6$ microcubes, and (e) their corresponding powder XRD pattern; (i) $ZnSn(OH)_6$ and (ii) $SnO_x/ZnSn(OH)_6$. All the peaks are indexed to the pure cubic phase and lattice parameter $a = 7.80$ Å, the space group of $Pn\bar{3}$ (201). (f) Transmission FT-IR spectra of (i) $ZnSn(OH)_6$ and (ii) $SnO_x/ZnSn(OH)_6$ materials.

and $SnO_x/ZnSn(OH)_6$ (Fig. 1e) clearly indicate the crystalline nature of these cuboids. But there were no additional peaks for the SnO_2 phase or for other phases in $SnO_x/ZnSn(OH)_6$. This indicates that the SnO_x nanoparticles are amorphous in nature. Both the materials displayed primary peaks at 19.93, 22.99, 32.70, 36.68, 38.59, 40.32, 46.91, 52.80, and 58.17° corresponding to the (111), (200), (220), (310), (311), (222), (400), (420), and (422) planes, respectively, of the zinc hydroxystannate phase.[44] These diffraction peaks are matched to a pure cubic phase with lattice parameter $a = b = c = 7.800$ Å and the space group of $Pn\bar{3}$ (JCPDS no. 96-901-2079). The distinct diffraction patterns observed in the as-prepared samples clearly indicate that the sample is crystalline in nature and possesses high purity. The material [$ZnSn(OH)_6$] synthesized using microwave radiation was crystalline in nature and composed of ZnO_6 octahedra and SnO_6 octahedra (JCPDS no. 96-901-2079).

Additionally, FT-IR spectroscopy measurements were conducted to analyze the bonding environment of the materials.[50,51] The FT-IR spectra in Fig. 1f show the molecular vibrations between Zn, Sn, O and H. Fig. 1f shows the FT-IR spectra of the $ZnSn(OH)_6$ material. The bands of absorption are detected at 3210, 1628, 1172, 1104, 777, and 536 cm^{-1}. These bands demonstrate strong correlation with the $ZnSn(OH)_6$ material previously reported.[52,53] The infrared spectrum displays a prominent, narrow band at approximately 3210 cm^{-1}, indicating the presence of O–H stretching vibration. The small band at 1628 cm^{-1} is ascribed to the adsorbed water molecules on the materials. The sharp band at 1172 cm^{-1} may arise due to the Sn–OH bending vibrations.[53] The sharp band at 1108 cm^{-1} arises due to the out-of-plane deformation vibration of Zn–OH, while the stretching vibrations of Sn–O–Sn are observed at 536 cm^{-1} and 777 cm^{-1}.[52]

Fig. 2 and S1 show high-resolution transmission electron microscopy (HR TEM) images of $ZnSn(OH)_6$ and $SnO_x/ZnSn(OH)_6$ materials at different magnifications. In Fig. 2a, the high-resolution TEM image shows that $ZnSn(OH)_6$ is a cuboid-shaped particle with a length of 0.7 μm. Fig. 2b and c also show a similar texture at high magnifications for the $ZnSn(OH)_6$ material. Even after the loading of SnO_x, the particle's cuboid shape remains intact, with small SnO_x nanoparticles deposited

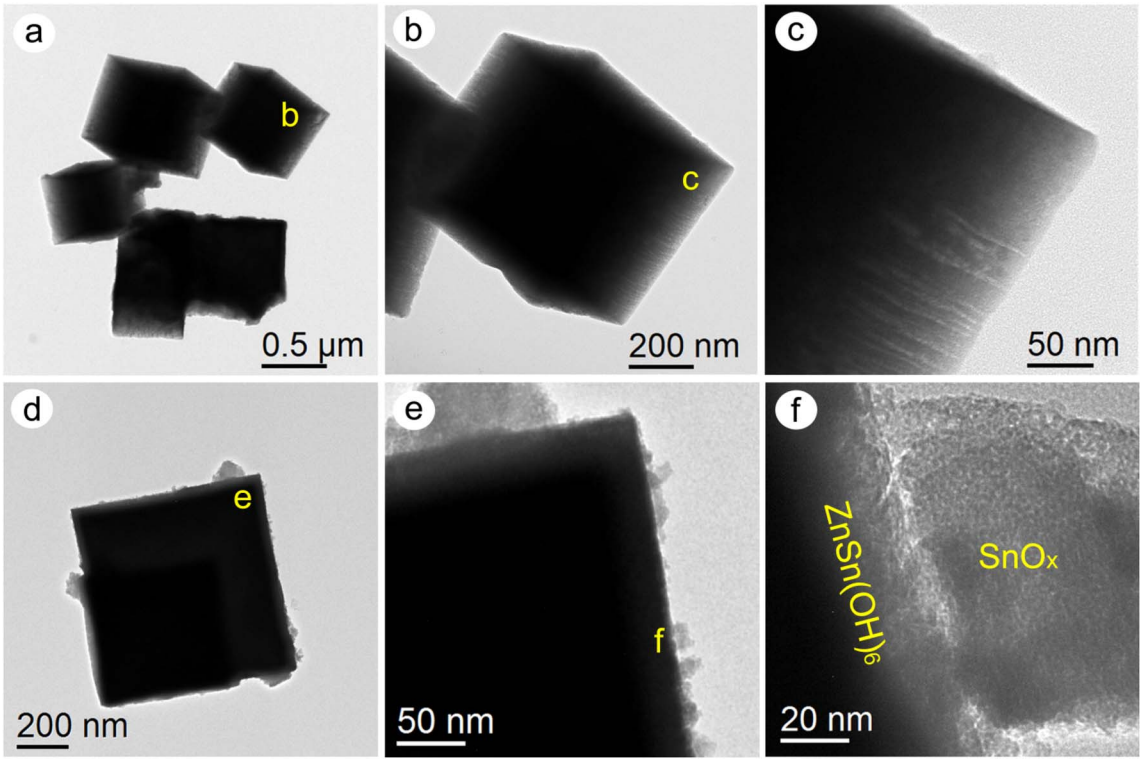

Fig. 2 High-resolution TEM images of (a–c) $ZnSn(OH)_6$ and (d–f) $SnO_x/ZnSn(OH)_6$ microcubes at different magnifications.

on the surfaces (Fig. 2d). The surface SnO_x is more clearly visible in the highly magnified images in Fig. 2e and f. Furthermore, the presence of SnO_x on the surface of the $ZnSn(OH)_6$ material was established by elemental mapping (Fig. S1).

2.2 Surface analysis

To investigate the surface chemical composition of the $ZnSn(OH)_6$ microcubes, X-ray photoelectron spectroscopy (XPS) analysis was performed. For the $ZnSn(OH)_6$ and $SnO_x/ZnSn(OH)_6$ materials, the survey profile, high-resolution XPS spectra of Zn 2p core level, Sn 3d core level and O 1s core level are shown in Fig. S2 and 3. The survey profile of $ZnSn(OH)_6$ and $SnO_x/ZnSn(OH)_6$ microcubes across the 0–1200 eV region is depicted in Fig. S2 showing the presence of Zn, Sn and O elements. For $ZnSn(OH)_6$, the high-resolution Zn 2p spectrum (Fig. 3a) displayed two broad peaks at 1021.74 eV for Zn $2p_{3/2}$ and 1044.84 eV for Zn $2p_{1/2}$.[53,54] The spin–orbit splitting of 23.1 eV is indicative of the Zn^{2+} oxidation state in the $ZnSn(OH)_6$ microcubes.[55,56] The high-resolution Sn 3d spectrum (Fig. 3b) displayed peaks at 486.73 eV for Sn $3d_{5/2}$ and 495.29 eV for Sn $3d_{3/2}$.[53,54] The spin–orbit splitting of 8.56 eV is indicative of the Sn^{4+} oxidation state in the $ZnSn(OH)_6$ microcubes.[55] The Zn 2p peak (Fig. 3d) and Sn 3d peak (Fig. 3e) in $SnO_x/ZnSn(OH)_6$ demonstrate similar observation to $ZnSn(OH)_6$. The O 1s peak in $ZnSn(OH)_6$ microcubes displays asymmetry and a noticeable shoulder, which can be further divided into three distinct Gaussian–Lorentzian components (Fig. 3c). The main peak of O 1s at 531.45 eV is related to oxygen components (*e.g.*, OH) within $ZnSn(OH)_6$, adsorbed water nearly at 533.14 eV and the other one at around 530.01 eV is assigned to oxygen in metal oxides (*e.g.*, Sn–O–Zn).[54] Upon SnO_x loading on $ZnSn(OH)_6$, the population of Sn–O–Zn and Sn–O–Sn increases compared to Sn/Zn–OH which was reflected in the O 1s spectra (Fig. 3f) of $SnO_x/ZnSn(OH)_6$. The elemental composition of the $ZnSn(OH)_6$ surface was analyzed using XPS peak areas to determine the semi-quantitative atomic percentages due to its surface sensitivity (~10 nm). The $ZnSn(OH)_6$ microcubes were found to contain 10.40% Zn, 13.08% Sn, and 76.52% O. The $SnO_x/ZnSn(OH)_6$ microcubes were found to contain 9.61% Zn, 19.75% Sn, and 70.63% O. To further verify the composition, we conducted elemental mapping and energy-dispersive X-ray spectroscopy (EDX) analysis (surface-sensitive ~1–3 μm). The elemental mapping and EDX spectrum of Zn, Sn, and O are presented in Fig. 4 and S3, revealing the presence of Zn, Sn, and O throughout the microcubes. The elemental compositions of $ZnSn(OH)_6$ using EDX are 13.37% Zn, 11.45% Sn, and 75.18% O. After loading SnO_x onto the $ZnSn(OH)_6$ surface, the composition changed to 10.41% Zn, 8.34% Sn, and 81.25% O. Both XPS and EDX show similar results of the $ZnSn(OH)_6$ composition, which align with theoretical values.

Significant discrepancy between the EDS and XPS data for $ZnSn(OH)_6$ (*e.g.*, Sn/Zn ratio) is expected due to their different sampling depths and surface-sensitivities. But both semi-quantitative analyses show similar results (*e.g.*, Sn/Zn ratio) and the calculations in Fig. S3 show that the amount of Sn and O increased in the $SnO_x/ZnSn(OH)_6$ material with respect to $ZnSn(OH)_6$. Additionally, we conducted measurements of the surface properties, oxygen vacancies, and defects, utilizing electron spin resonance (ESR) techniques. The ESR spectra

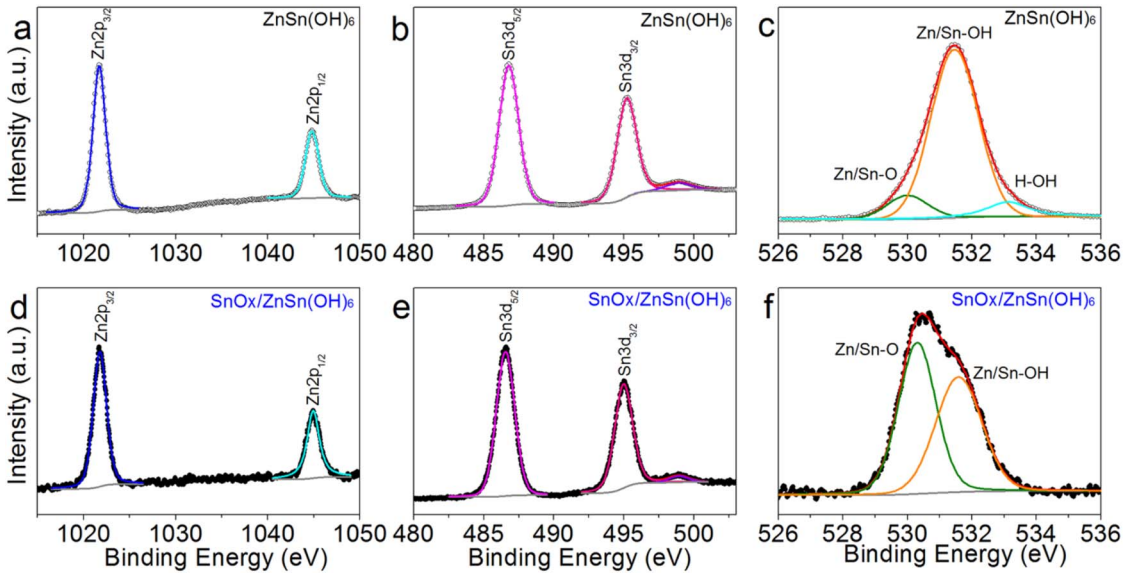

Fig. 3 High-resolution XPS analysis of the $ZnSn(OH)_6$ and $SnO_x/ZnSn(OH)_6$ microcubes showing (a and d) core level Zn 2p, (b and e) Sn 3d and (c and f) O 1s regions independently. The black dots are the experimental data, and the red line is the sum of the deconvoluted components, respectively.

provide compelling evidence of a higher concentration of oxygen vacancies (OVs) in $SnO_x/ZnSn(OH)_6$ compared to $ZnSn(OH)_6$, with a *g*-value of 2.04 (Fig. S4).[57,58] Under light illumination, $SnO_x/ZnSn(OH)_6$ exhibits a significantly higher peak intensity, indicating a greater ease of electron formation upon photoirradiation.[58] This observation highlights its superior ability to generate photoinduced electrons, which positively influences its photoactivity.

2.3 Electronic structure and electrochemical study

Fig. 5a reveals that the $ZnSn(OH)_6$ microcubes exhibit strong ultraviolet light absorption at approximately 215 and 250 nm, with a band gap energy of 3.98 eV (as shown in the inset of Fig. 5a).[53] On the other hand, the $SnO_x/ZnSn(OH)_6$ microcubes demonstrate strong ultraviolet light absorption around 215 and 254 nm, with a slightly lower band gap energy of 3.90 eV (as depicted in the inset of Fig. 5a). A comparison between $ZnSn(OH)_6$ and $SnO_x/ZnSn(OH)_6$ reveals that the adsorption spectra of the latter shifts to longer wavelengths due to the deposition of SnO_x on the surface $ZnSn(OH)_6$ cubes, resulting in a lower band gap energy. In Fig. S5 and 5b, the electrochemical Mott–Schottky plots of $ZnSn(OH)_6$ and $SnO_x/ZnSn(OH)_6$ materials are presented, respectively. Both plots exhibit n-type responses, and the flat band potential of the conduction band (CB) of $ZnSn(OH)_6$ and $SnO_x/ZnSn(OH)_6$ was calculated from

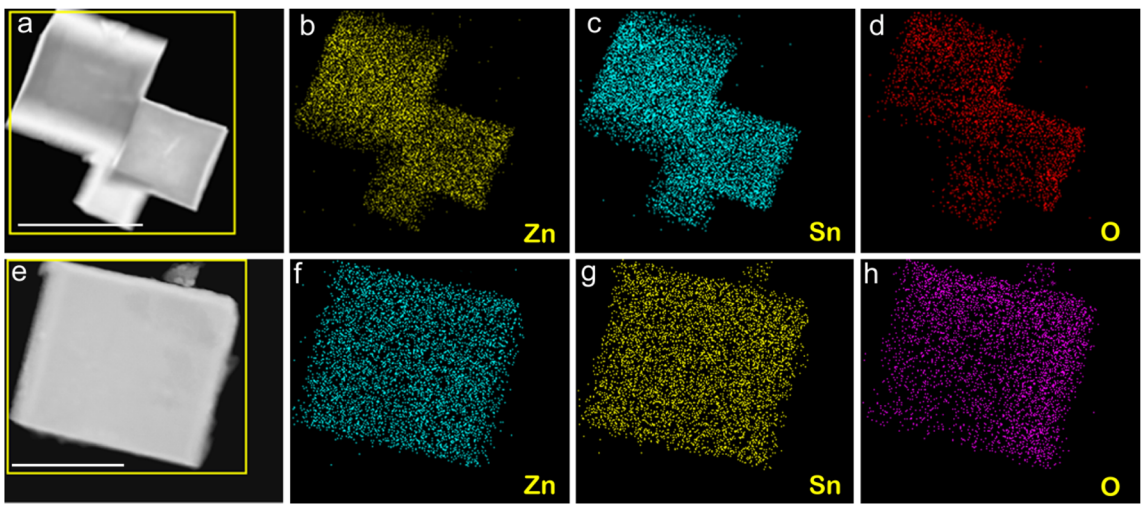

Fig. 4 Dark-field STEM image of (a) $ZnSn(OH)_6$ microcubes (scale bar 900 nm) and elemental mapping of (b) Zn (yellow), (c) Sn (cyan), and (d) O (red). Dark-field STEM image of (e) $SnO_x/ZnSn(OH)_6$ microcubes (scale bar 400 nm) and elemental mapping of (f) Zn (cyan), (g) Sn (yellow), and (h) O (magenta).

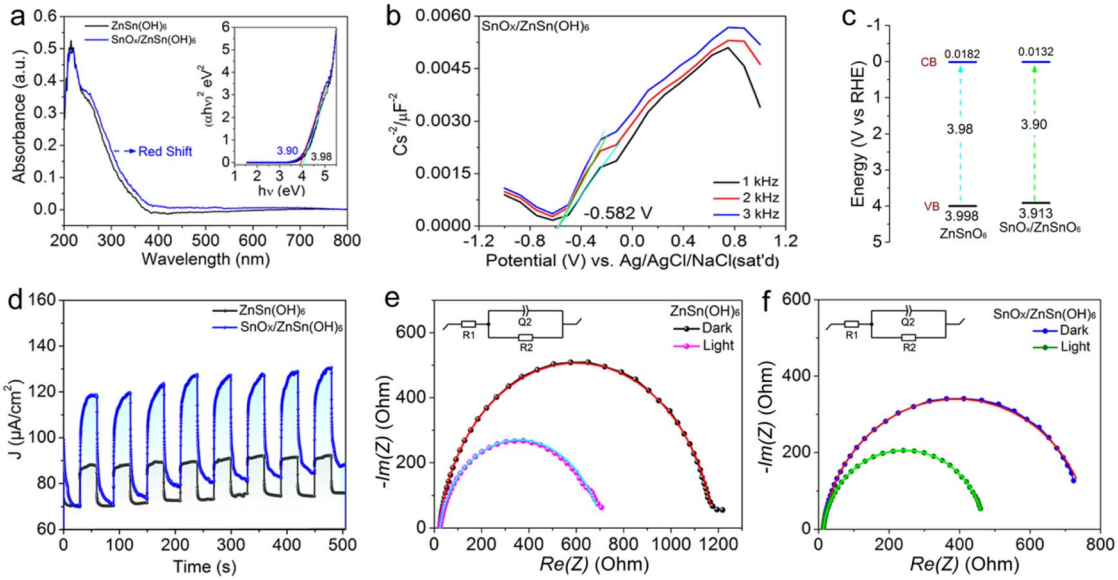

Fig. 5 (a) UV-Vis DRS spectra and corresponding Tauc plot (inset) used to estimate the bandgap of $ZnSn(OH)_6$ and $SnO_x/ZnSn(OH)_6$. (b) Mott–Schottky plots of $SnO_x/ZnSn(OH)_6$ in different frequencies. (c) Electronic band structure of $ZnSn(OH)_6$ and $SnO_x/ZnSn(OH)_6$. (d) Photocurrent responses of $ZnSn(OH)_6$ and $SnO_x/ZnSn(OH)_6$. (e) EIS Nyquist plots for $ZnSn(OH)_6$ microcubes in the presence and absence of light (inset equivalent circuit) and (f) EIS Nyquist plots for $SnO_x/ZnSn(OH)_6$ in the presence and absence of light (300 watt Xe lamp) (inset equivalent circuit).

the intercepts on the horizontal axis. The flat band potential of $ZnSn(OH)_6$ was determined to be −0.577 V (0.0182 V *vs.* RHE), while for $SnO_x/ZnSn(OH)_6$, it was found to be −0.582 V *vs.* Ag/AgCl (0.0132 V *vs.* RHE).[53] Based on the results presented above, the band energy structures of $ZnSn(OH)_6$ and $SnO_x/ZnSn(OH)_6$ are proposed, as depicted in Fig. 5c. The highest conduction band potential of both $ZnSn(OH)_6$ and $SnO_x/ZnSn(OH)_6$ materials shows a positive value close to the H^+/H_2 potential. To investigate the rates of charge transfer and the efficiency of separating photogenerated electrons and holes, transient photocurrent response and impedance spectroscopic (EIS) measurements were conducted. The transient photocurrent density of $ZnSn(OH)_6$ and SnO_x decorated $ZnSn(OH)_6$ is shown in Fig. 5d. Typically, the intensity of the photocurrent response is directly linked to the efficiency of separating photogenerated electrons and holes. This finding confirms that $SnO_x/ZnSn(OH)_6$ effectively inhibits the recombination of charge pairs better than $ZnSn(OH)_6$, which aligns with the results obtained from the EIS analysis. The results indicate that the presence of SnO_x on the surface of $ZnSn(OH)_6$ forms a heterojunction and effectively reduces recombination rates. This phenomenon is visually represented in Fig. 5e and f, where it can be observed that $ZnSn(OH)_6$ and $SnO_x/ZnSn(OH)_6$ display a smaller semicircular radius on the Nyquist curve when exposed to light as opposed to darkness. This reduction in radius suggests a decrease in interfacial charge transfer resistance under light conditions, which is highly beneficial for facilitating electron and hole transfer processes. Furthermore, the steady-state photoluminescence (PL) spectrum was utilized to assess the separation efficiency of the photogenerated carriers (see Fig. S6).[57,59] Notably, the fluorescence intensity of $SnO_x/ZnSn(OH)_6$ was found to be lower than that of $ZnSn(OH)_6$. This observation indicates that the incorporation of SnO_x effectively mitigates the recombination of photogenerated carriers, likely due to the presence of oxygen vacancies and defects.[57,59] The impedance spectra were meticulously analyzed using the equivalent Randles circuit $R_1 + Q_2/R_2$, with R_1 representing electrolytic resistance, R_2 representing charge transfer resistance, and Q_2 representing constant phase elements.[60] The values of R_1, Q_2 and R_2 under both light and dark conditions are detailed in Table S1. The charge transfer resistance (R_2) value of $ZnSn(OH)_6$ under light conditions is 644.3 Ω, which is significantly lower than the value observed in the dark, which was 1155.0 Ω. Additionally, the loading of SnO_x on $ZnSn(OH)_6$ resulted in further reduction in charge transfer resistance under both dark and light conditions. The R_2 value of $SnO_x/ZnSn(OH)_6$ under light conditions is 464.1 Ω, which is significantly lower than the value observed in the dark, which was 746.0 Ω. To evaluate charge separation and interfacial charge transfer resistance under photocatalytic reaction conditions (*i.e.*, under 254 nm light), we conducted photocurrent generation and EIS Nyquist measurements. The findings are summarized in Fig. S7 and Table S1. The results demonstrate that SnO_x-coated $ZnSn(OH)_6$ exhibits a higher photocurrent density compared to $ZnSn(OH)_6$. Notably, both $ZnSn(OH)_6$ and $SnO_x/ZnSn(OH)_6$ show a reduced semicircular radius on the Nyquist plot when illuminated with 254 nm light, in contrast to measurements taken in darkness. This reduction in radius indicates a decrease in interfacial charge transfer resistance under light conditions, which significantly facilitates the transfer processes of electrons and holes.

2.4 Photocatalytic activity

The optical and electrochemical properties observed in $SnO_x/ZnSn(OH)_6$ have inspired us to further explore its potential as

Table 1 Optimization studies for photocatalytic cycloaddition of CO_2 and styrene oxide by $SnO_x/ZnSn(OH)_6$ microcubes under different conditions

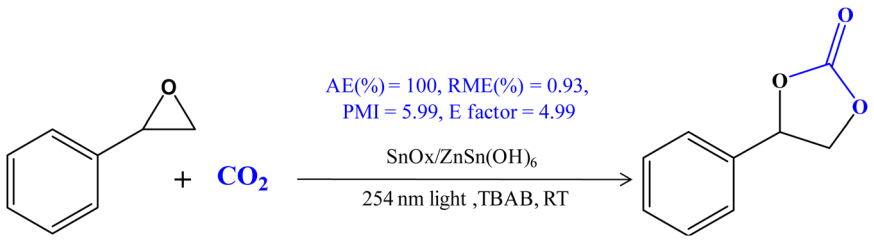

Entry	Variation from the standard conditions	Time (h)	Yield (%)	Rate (μmol h^{-1})	Activity (μmol h^{-1} g^{-1})	AQY[b] × 10^5
1	Standard conditions[a]	12	93.0	232.5	4650.0	722.89
2	No $SnO_x/ZnSn(OH)_6$ (no catalyst, TBAB only)	12	19.0	47.5	950.0	147.69
3	No light (dark)	12	15.6	39.0	780.0	121.26
4	No CO_2 (Ar)	12	0.00	0.0	0.0	0.00
5	No TBAB	12	0.00	0.0	0.0	0.00
6	$ZnSn(OH)_6$	12	74.0	185	3700.0	575.20
7	ZnO	12	53.0	132.5	2650.0	411.97
8	SnO_2	12	29.0	72.5	1450.0	225.42
9	Acetonitrile	12	53.0	132.5	2650.0	411.97
10	DMF	12	18.0	45.0	900.0	139.91
11	Ethylene glycol	12	22.0	55.0	1100.0	171.01
12	PEG 600	12	93.0	232.5	4650.0	722.89
13	Ethanol	12	39.0	97.5	1950.0	303.15
14	H_2O + ethanol	12	59.0	147.5	2950.0	458.61
15	H_2O	12	8.0	20.0	400.0	62.18
16	Without solvent	12	73.0	182.5	3650.0	567.43
17	White light[c]	12	19.0	47.5	950.0	—
18	Simulated solar light (<420 nm)[d]	06	24.0	120.0	2400.0	—

[a] Standard conditions: $SnO_x/ZnSn(OH)_6$ catalyst (50 mg), styrene oxide (3 mmol), PEG 600 (2 mL), 1 atm CO_2 balloon, TBAB (0.3 mmol), 8 watt UV light (254 nm), room temperature, 12 h (PEG – polyethylene glycol). [b] Apparent quantum yield. [c] The standard reaction was carried out in white light (50 W). [d] Simulated solar light (using a 420 nm cut-off filter). AE, RME, PMI and *E* factor are green chemistry metrics.

a heterogeneous photocatalyst for the CO_2 cycloaddition reaction. The CO_2 cycloaddition reaction with styrene oxide was chosen as a representative model for our initial optimization experiments. Remarkably, this reaction resulted in 93% yield of the desired product, styrene carbonate, when employing $SnO_x/ZnSn(OH)_6$ as the photocatalyst, TBAB as the co-catalyst, a 1 atm CO_2 balloon as the source of CO_2, and PEG 600 as the solvent, all under the influence of 8 watt UV light (254 nm) at room temperature (Table 1, entry 1). The 8 watt UV light (254 nm) was chosen based on the catalyst's absorption edge (Fig. 5a). The optimization conditions and time courses of the reaction are detailed in Table 1. Furthermore, the product of the reaction was thoroughly characterized using ^1H and ^{13}C NMR spectroscopy.

After 6 h of reaction time, 72% formation of the product was observed through ^1H NMR analysis (see the SI, Fig. S8 and S9). This percentage steadily increased as the reaction time progressed, ultimately reaching complete conversion after 12 h of irradiation. The isolated yield was an impressive 93% (see SI, Fig. S8 and S10). In order to comprehend the significance of the $SnO_x/ZnSn(OH)_6$ photocatalyst in this cycloaddition process, a control experiment was carried out without the presence of $SnO_x/ZnSn(OH)_6$ (Table 1, entry 2). The NMR analysis (see SI, Fig. S11) of the reaction mixture revealed a decreased conversion of the reactant to the product, indicating the crucial role of $SnO_x/ZnSn(OH)_6$ in facilitating this cycloaddition reaction. Without light, the catalyst yields 15.6% (see Table 1, entry 3, SI, Fig. S12), implying that it contains both acidic and basic sites. Similarly, control experiments were conducted in the absence of CO_2 (Table 1, entry 4), and TBAB (Table 1, entry 5), resulting in no detectable product formation. Additionally, a time-resolved light-on/light-off experiment was carried out (see the SI, Fig. S13), which conclusively demonstrated that the reaction only occurred when the light was on. The rate of the reaction displayed a first-order dependence on the epoxide (Fig. S14). This observation strongly suggests that the reaction follows a photocatalytic pathway.

Various catalysts, such as $ZnSn(OH)_6$ (Table 1, entry 6, Fig. S15), ZnO (Table 1, entry 7, Fig. S16), and SnO_2 (Table 1, entry 8, Fig. S17), were tested instead of $SnO_x/ZnSn(OH)_6$. However, these alternatives resulted in poor product formation. The activity of the catalyst was compared with several reported catalysts and results are shown in Table S2.[61,62] The reaction was also conducted in various solvent systems (Table 1, entry 9–15),

revealing that PEG 600 is the most effective solvent for this cycloaddition reaction. Wu *et al.* demonstrated that PEGs with varying molecular weights significantly influenced the outcomes of the cycloaddition reaction between CO_2 and propylene oxide.[63] Their findings indicate that the yield of propylene carbonate decreases markedly as the PEG chain length increases from PEG 200 to PEG 1000, likely due to mass-transport limitations. The reaction was also carried out without the use of any solvent, resulting in a yield of 73% (Table 1, entry 16). The reaction was also carried out with white light (50 W) and simulated solar light (using a 420 nm cut-off filter), resulting in a poor conversion of styrene oxide to cyclic carbonate (Table 1, entries 17 and 18). These results show the wide band gap limitation of the catalyst. In addition to optimizing the process, we have also calculated the rate (μmol h^{-1}), activity (μmol h^{-1} g^{-1}), and apparent quantum yield which are detailed in Table 1. Different quantities of $SnO_x/ZnSn(OH)_6$ were evaluated, with the results depicted in Fig. 6a and Table S3 (entry 1–5). Furthermore, the catalyst's reusability was assessed, showing that it maintained photocatalytic activity for up to six consecutive cycles (Fig. 6b), highlighting its potential for reuse. The compound $SnO_x/ZnSn(OH)_6$ can be effortlessly isolated from the reaction mixture through centrifugation and can be directly utilized in subsequent runs without the need for any additional treatment or reactivation process. The recycled $SnO_x/ZnSn(OH)_6$ maintained its initial structure and crystallinity, as evidenced by the unchanged FT-IR, powder XRD, SEM, Nyquist and XPS analysis results (see the SI, Fig. S18, S19 and Table S4). FT-IR and XRD analyses demonstrate good structural stability. Additionally, XPS analysis conducted before and after the reaction reveals that the oxidation states of the metals remain unchanged. This suggests the good stability of the $SnO_x/ZnSn(OH)_6$ photocatalyst.

After optimizing the conditions, the potential of the $SnO_x/ZnSn(OH)_6$ photocatalyst for synthesizing cyclic organic carbonates was investigated by testing various sources of epoxides. The results, as displayed in Table 2, demonstrate that with the addition of a small amount of the $SnO_x/ZnSn(OH)_6$ catalyst, a range of epoxy substrates successfully produced the desired products with high isolated yields ranging from 87% to 95% (Table 2, entries 1–6). The reaction exhibited high compatibility with both aromatic and aliphatic epoxides. The results presented here showcase the promising potential of the $SnO_x/ZnSn(OH)_6$ photocatalyst for practical applications.

Literature indicates that researchers have delved into the mechanism of the CO_2 cycloaddition reaction. Several groups have proposed that epoxides are oxidized by photogenerated holes to form epoxides$^{\bullet+}$, while CO_2 is reduced by photogenerated electrons to $CO_2^{\bullet-}$. These species then combine in the presence of a halide co-catalyst to create an organic carbonate.[64] However, other researchers have suggested that epoxides are actually reduced to epoxides$^{\bullet-}$ and that CO_2 is neither reduced nor oxidized in this process.[61]

In order to gain a comprehensive understanding of the CO_2 cycloaddition reaction mechanism involved in this photocatalysis process, a series of meticulously controlled experiments were carried out and carefully monitored using ^1H NMR analysis. The reactions were executed under the most optimized conditions, in the presence of $AgNO_3$ (electron scavenger), KI (hole scavenger), $Na_2C_2O_4$ (hole scavenger), and 5,5-dimethyl-1-pyrroline-*N*-oxide (DMPO) (radical scavenger) (see Table S5 and Fig. 7a for details). The presence of either $AgNO_3$ or $Na_2C_2O_4$ resulted in a decrease in product formation (see Fig. S20 and S21). This suggests that both reductive electrons and oxidative holes play a role in the photocatalytic process. Additionally, the presence of DMPO led to a significant decrease in the yield of the desired product by 35%, indicating that the reaction follows a radical pathway (see Fig. S22). The anomalous behavior observed when using KI as a hole scavenger will be discussed later.

The results from linear sweep voltammetry (LSV) curves in the potential range −0.4 to −1.2 V *vs.* RHE indicate that $SnO_x/ZnSn(OH)_6$ exhibited a higher current response under CO_2 in the presence of light compared to under an argon atmosphere (see Fig. 7b). This suggests that the catalyst has the capability for CO_2 reduction and the current density increases due to CO_2 to $CO_2^{\bullet-}$ conversion.[65,66] Subsequently, the cyclic voltammetry (CV) of $SnO_x/ZnSn(OH)_6$ was examined in argon saturated and CO_2 saturated 0.5 M Na_2SO_4 electrolyte at a scan rate of 10 mV s^{-1} in the dark (see Fig. 7c).[67] The results from linear sweep voltammetry (LSV) curves in the potential range 0.6 to 1.6 V *vs.* RHE indicate that $SnO_x/ZnSn(OH)_6$ exhibited a higher current

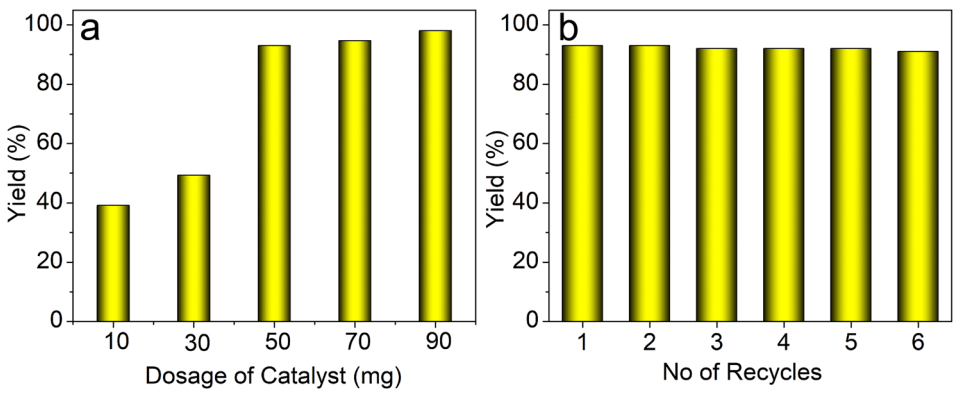

Fig. 6 (a) Amount of $SnO_x/ZnSn(OH)_6$ variation and (b) recyclability of $SnO_x/ZnSn(OH)_6$. The reactions were performed under standard conditions as shown in Table 1, entry 1.

Table 2 $SnO_x/ZnSn(OH)_6$ catalyzed CO_2 cycloaddition reaction with different epoxides to cyclic organic carbonates[a]

Entry	Reactant	Product	Time (h)	Yield (%) (SD)	AQY × 10^5
1	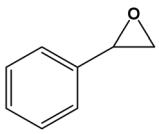	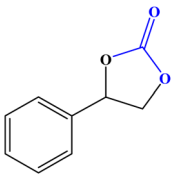	12	94.00 (1)	730.66
2	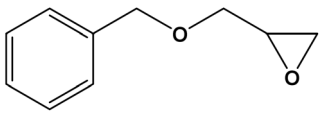	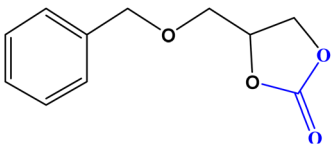	12	94.66 (0.33)	735.79
3	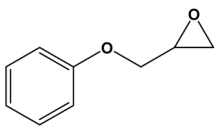	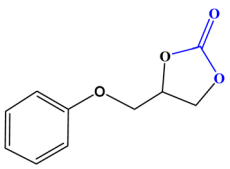	12	94.50 (0.25)	734.55
4	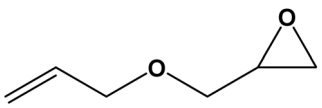	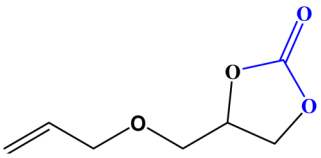	12	91.50 (0.375)	711.23
5	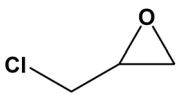	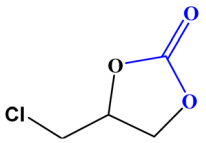	12	89.33 (2.33)	694.36
6	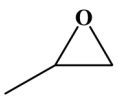	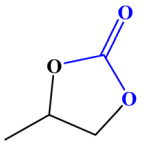	12	87.00 (1)	676.25

[a] Reaction conditions: $SnO_x/ZnSn(OH)_6$ catalyst (50 mg), epoxide (3 mmol), PEG 600 (2 mL), 1 atm CO_2, TBAB (0.3 mmol), 8 watt UV light (254 nm), room temperature, 12 h. SD-standard deviation, reactions were performed three times.

response in the presence of styrene oxide (see Fig. 7g). This suggests that the epoxides are oxidized to form epoxides$^{\bullet+}$. Recently, Zhang and co-workers identified the epoxide$^{\bullet+}$ radical generation for CO_2 cycloaddition reaction by ESR analysis, with TEMPO, DMPO, and MNP as spin trapping agents.[68] Fig. 7d presents the ESR spectrum of the $SnO_x/ZnSn(OH)_6$ microcubes, revealing an anisotropic one-line pattern with a *g*-value of 2.04. Upon the introduction of CO_2 (DMPO–$CO_2^{\bullet-}$, a_N = 14.1 & 14.0, see Fig. 7e) or styrene oxide (DMPO–epoxyalkyl radical, a_N = 14.1 & 13.9, see Fig. 7f) into the $SnO_x/ZnSn(OH)_6$ and DMPO system under 254 nm light irradiation, the signal attenuation transformed into a sharp, isotropic three-line pattern characteristic of a nitroxide radical (Fig. S23). This observation indicates an increased separation and transfer of photogenerated electrons and holes from $SnO_x/ZnSn(OH)_6$ to the reactants (CO_2 and styrene oxide) when exposed to light. Furthermore, the role of the co-catalyst was examined (Fig. 7h). TBAB only can perform the reaction with a low yield (Table 1, entry 2). However, on addition of KI as a hole scavenger (*i.e.*, TBAB & KI both are present, Fig. S24) in the reaction, the yield of the product increased. But when $Na_2C_2O_4$ was used as the hole scavenger in the reaction, the yield of the product decreased. This implies that a halide has a relevant role in the reaction. So, we used KI, KBr, and TBAI instead of TBAB, the reaction showed 99, 37 and 87% yields respectively (see Fig. S25–S27). This implies that iodide shows better performance than bromide in the reaction. We also performed the reaction with KI only (without the catalyst); 50% conversion was observed in the ^{1}H NMR analysis (see Fig. S28). This suggests that KI as the catalyst has the capability for styrene oxide conversion. A similar observation was reported in the literature.[69,70]

According to our controlled experiments, electrochemical studies, and previous literature, a reaction mechanism is proposed, as shown in Fig. 7i. Styrene oxide was adsorbed onto

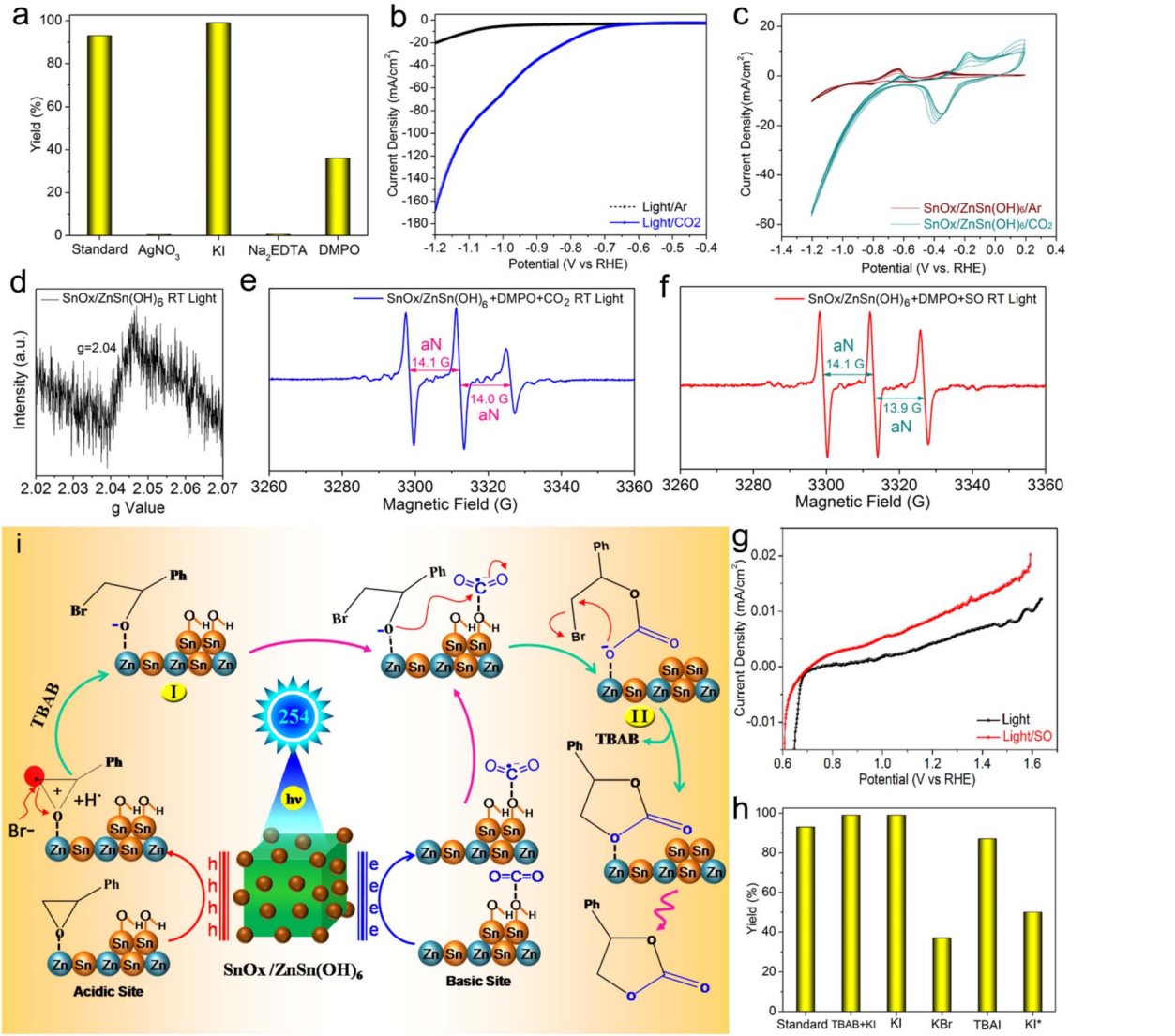

Fig. 7 (a) Controlled scavenger experiments. (b) LSV curves of $SnO_x/ZnSn(OH)_6$ in the argon saturated and CO_2 saturated 0.5 M Na_2SO_4 electrolyte at a scan rate of 10 mV s^{-1}. (c) CV curves of $SnO_x/ZnSn(OH)_6$ in the argon saturated and CO_2 saturated 0.5 M Na_2SO_4 electrolyte at a scan rate of 10 mV s^{-1}. ESR spectrum of (d) $SnO_x/ZnSn(OH)_6$ material, (e) $SnO_x/ZnSn(OH)_6$ with DMPO added under a CO_2 atmosphere in the presence of 254 nm UV light and (f) $SnO_x/ZnSn(OH)_6$ with DMPO added under styrene oxide in the presence of 254 nm UV light. (g) LSV curves of $SnO_x/ZnSn(OH)_6$ in the absence and presence of styrene oxide 0.1 M $[NBu_4][PF_6]$ CH_3CN solution at a scan rate of 10 mV s^{-1}. (h) Effect of different co-catalysts. (i) Proposed reaction mechanism.

the Zn/Sn species of the $SnO_x/ZnSn(OH)_6$ catalyst through oxygen atoms, while CO_2 was adsorbed at Lewis basic sites. When exposed to light, $SnO_x/ZnSn(OH)_6$ produced photogenerated electrons and holes. The photogenerated holes then oxidized styrene oxide, creating carbon-centered radicals with a positive charge. Following this, Br^- ions in TBAB attacked the less hindered carbon atom in styrene oxide through a nucleophilic attack, resulting in ring-opening and the formation of a bromopropoxy intermediate (I). At the same time, photogenerated electrons reduced CO_2 to $CO_2^{\bullet-}$ species, which then combined with the bromopropoxy intermediate (I) to form intermediate (II). Ultimately, the intramolecular cyclization of intermediate (II) led to the creation of styrene carbonate, regenerating the $SnO_x/ZnSn(OH)_6$ catalyst and TBAB in the process.

3. Conclusion

We have successfully developed a SnO_x-decorated $ZnSn(OH)_6$ catalyst for use in photocatalytic CO_2 cycloaddition reactions. The presence of SnO_x on the surface of $ZnSn(OH)_6$ makes it an ideal photocatalyst, as evidenced by high charge separation demonstrated through photocurrent density and Nyquist analysis. The $SnO_x/ZnSn(OH)_6$ catalyst exhibited outstanding catalytic performance, achieving approximately 93% conversion and a reaction rate of 4650 μmol g^{-1} h^{-1} in CO_2 cycloaddition reactions with styrene oxide under light irradiation. This performance was approximately 1.3, 1.8 and 2.1 times higher than that of the $ZnSn(OH)_6$, ZnO and SnO_2 catalyst respectively. The catalyst also demonstrated high yields (87–95%) when

tested with various substrates. Furthermore, the catalyst showed good recyclability, making it a promising option for sustainable catalytic processes.

4. Experimental section

4.1 Synthesis of zinc hydroxystannate microcubes [$ZnSn(OH)_6$]

Cuboid shaped zinc hydroxystannate was synthesized by a microwave assisted technique without any template. In a standard synthesis procedure, 1 mmol of $Zn(NO_3)_2 \cdot 6H_2O$ was dissolved in 20 mL of water and stirred for a few minutes. In a separate beaker, 1 mmol of $SnCl_4 \cdot 5H_2O$ was dissolved in 20 mL of water. The second solution was then slowly added to the first solution. The pH of the solution was adjusted to 8 by the dropwise addition of 1 (N) NaOH. The resultant mixture was stirred for 45 minutes at room temperature. After that the solution mixture was transferred into a polypropylene bottle and placed in a microwave reactor. The microwave power (Commercial Panasonic Microwave, model number NN-CT644M, level P100, 900 W) was set to 900 watt for 2 minutes (1 atm, temperature 100 °C). After the reaction, the bottle was allowed to cool to room temperature and the precipitate was collected by centrifugation. The sample was washed several times using water and ethanol.

4.2 Synthesis of SnO_x decorated $ZnSn(OH)_6$ microcubes [$SnO_x/ZnSn(OH)_6$]

100 mg as-synthesized $ZnSn(OH)_6$ powder was dispersed in 35 mL water and sonicated for 10 minutes. Then 10 mg $SnCl_4 \cdot 5H_2O$ was dissolved in 5 mL water. The solution was added to the former solution. The pH of the solution was adjusted to 8 with 2 (N) NaOH followed by sonication and stirring. The well-mixed solution was then transferred into a 50 mL polypropylene bottle and placed in a microwave reactor at 900 watt for 2 minutes (1 atm, temperature 100 °C). The final product was collected by centrifugation and washed with ethanol.

4.3 Catalytic activity

Herein, $SnO_x/ZnSn(OH)_6$ microcube catalysts were prepared and employed in the photocatalytic cycloaddition reaction of CO_2 and different epoxides at ambient pressure and room temperature. The catalytic experiments were conducted using a CO_2 balloon as the source of CO_2. In the catalytic reaction, a round bottom flask was used to combine 3 mmol of styrene oxide, 2 mL of PEG 600 solvent, and 0.3 mmol of TBAB. Subsequently, 50 mg of the $SnO_x/ZnSn(OH)_6$ catalyst was introduced into the solution, which was then sealed with a silicone rubber septum. CO_2 was purged into the solution using the CO_2 balloon connected with a stainless steel needle. The solution was stirred under a light illumination of 254 nm UV light (8 watt, Genei Make) at room temperature. The reaction progress was monitored using TLC. Once the reaction was complete, the catalyst was recovered and the product was obtained using a mixture of ethyl acetate and water. The products were then separated using column chromatography. The optimization of the reaction and different substrate scope results are listed in Tables 1, 2 and S3–S5. The products were analyzed using ^1H and ^{13}C NMR spectroscopy, as depicted in the SI file.

Author contributions

Soumita Sarkar: data curation, formal analysis, methodology, resources, software, validation, visualization, writing – original draft, writing – review & editing. Soumalya Banerjee: data curation, methodology, software, visualization, writing – review & editing. Sk Afsar Ali: data curation, methodology, software, validation, writing – review & editing. Sunny Sarkar: data curation, methodology, software, validation, writing – review & editing. Astam K. Patra: conceptualization, formal analysis, funding acquisition, investigation, project administration, resources, software, supervision, validation, visualization, writing – original draft, writing – review & editing.

Conflicts of interest

There are no conflicts to declare.

Data availability

The data supporting this article have been included as part of the supplementary information (SI). Data are also available upon request from the authors. Supplementary information: experimental details and different characterization experiments, XPS, EDX, EPR, Mott–Schottky plots, PL spectra, photocurrent responses of the catalyst under 254 nm light, green chemistry metrics, reaction kinetics, light-on/light-off experiment, assessment of quenchers, ^1H and ^{13}C NMR spectra, and photocatalyst performance comparison. See DOI: https://doi.org/10.1039/d5su00789e.

Acknowledgements

Ms Soumita Sarkar acknowledges the Swami Vivekananda Merit Cum Means PhD Scholarship, Government of West Bengal, India. Mr Soumalya Banerjee and Mr Sk Afsar Ali acknowledge the University Grants Commission (UGC), Government of India for the Junior Research Fellowship. Mr Sunny Sarkar acknowledges University of Kalyani for Fellowship and Personal Research Grant. Dr A. K. Patra acknowledges the Anusandhan National Research Foundation (ANRF), Government of India for funding (File No. EEQ/2021/000008). Dr A. K. Patra also acknowledges the University of Kalyani for providing the basic infrastructure. All authors acknowledge IACS Kolkata and IISER Kolkata for instrument facility. The help received from DST PURSE II grant of the University of Kalyani and DST FIST LEVEL II (SR/FST/CS-II/2019/96) grant of the Department of Chemistry, University of Kalyani is also acknowledged by Dr A. K. Patra.

References

1 J. Artz, T. E. Müller, K. Thenert, J. Kleinekorte, R. Meys, A. Sternberg, A. Bardow and W. Leitner, *Chem. Rev.*, 2018, **118**, 434–504.

2 L. Qiu, B. Li, J. Hu, A. Ganesan, S. Pramanik, J. T. Damron, E. Li, D.-e. Jiang, S. M. Mahurin, I. Popovs, C. A. Steren, J. Fan, Z. Yang and S. Dai, *J. Am. Chem. Soc.*, 2024, **146**, 29588–29598.
3 M. Wang, M. Yabushita, K. Okuma, T. Shono, Y. Nakagawa and K. Tomishige, *Green Chem.*, 2025, **27**, 7174–7190.
4 A. J. Kamphuis, F. Picchioni and P. P. Pescarmona, *Green Chem.*, 2019, **21**, 406–448.
5 Y. Feng and J. Yao, *Sep. Purif. Technol.*, 2025, **356**, 130027.
6 A. J. David and A. Das, *Green Chem.*, 2025, **27**, 851–862.
7 J. Zhao, Z. Li, P. Wang, P. Miao, R. Shi, G. I. N. Waterhouse, L.-Z. Wu and T. Zhang, *Matter*, 2024, **7**, 1696–1709.
8 M. Sain, D. Dey, R. Sen and S. Chowdhury, *RSC Sustainability*, 2025, **3**, 2733–2749.
9 G. Fu, M. Jiang, J. Liu, K. Zhang, Y. Hu, Y. Xiong, A. Tao, Z. Tie and Z. Jin, *Nano Lett.*, 2021, **21**, 8824–8830.
10 W. Neamsung, N. Kitjanukit, A. Karawek, N. Chongkol, N. Lertthanaphol, P. Chotngamkhum, K. Khumsupa, P. Phadungbut, W. Jonglertjunya, P. Kim-Lohsoontorn and S. Srinives, *RSC Sustainability*, 2025, **3**, 3520–3529.
11 G. Yang, Q. Wang, Y. Kuwahara, K. Mori and H. Yamashita, *Chem Bio Eng.*, 2024, **1**, 289–311.
12 Q. Chen, H. Yu, H. Li, K. Liu and M. Liu, *Chem. Commun.*, 2025, **61**, 19403–19420.
13 L. Eisele, B. Hulaj, M. Podsednik, F. Laudani, P. Ayala, A. Cherevan, A. Foelske, A. Limbeck, D. Eder and K. Bica-Schröder, *RSC Sustainability*, 2024, **2**, 2524–2531.
14 Y. Xiong, W. Zhao, D. Gu, Z. Tie, W. Zhang and Z. Jin, *Nano Lett.*, 2023, **23**, 4876–4884.
15 L. Qiu, N. Mokhtarinori, H. Liu, D.-e. Jiang, Z. Yang and S. Dai, *Mater. Today Energy*, 2025, **47**, 101740.
16 B. Schäffner, F. Schäffner, S. P. Verevkin and A. Börner, *Chem. Rev.*, 2010, **110**, 4554–4581.
17 W. Yu, E. Maynard, V. Chiaradia, M. C. Arno and A. P. Dove, *Chem. Rev.*, 2021, **121**, 10865–10907.
18 P. Markewitz, W. Kuckshinrichs, W. Leitner, J. Linssen, P. Zapp, R. Bongartz, A. Schreiber and T. E. Müller, *Energy Environ. Sci.*, 2012, **5**, 7281–7305.
19 C. Martín, G. Fiorani and A. W. Kleij, *ACS Catal.*, 2015, **5**, 1353–1370.
20 L. A. Siddig, R. H. Alzard, H. L. Nguyen and A. Alzamly, *Inorg. Chem. Commun.*, 2022, **142**, 109672.
21 H. Eliasson, Y.-T. Chiang, T. P. Araújo, X. Li, R. Erni, S. Mitchell and J. Pérez-Ramírez, *Adv. Mater.*, 2025, **37**, 2419859.
22 Y. Ge, A. J. Martín, M. Suvarna, T. Zou, F. Krumeich and J. Pérez-Ramírez, *Appl. Catal., B*, 2025, **378**, 125578.
23 J. Zhang, C. Shang, Z. An, Y. Zhu, H. Song, Z. Chai, X. Shu, L. Zheng and J. He, *Angew. Chem., Int. Ed.*, 2023, **62**, e202312068.
24 S. P, J. John, T. P. D. Rajan, G. M. Anilkumar, T. Yamaguchi, S. C. Pillai and U. S. Hareesh, *J. Mater. Chem. A*, 2023, **11**, 8599–8646.
25 J. Koppe, A. V. Yakimov, D. Gioffrè, M.-E. Usteri, T. Vosegaard, G. Pintacuda, A. Lesage, A. J. Pell, S. Mitchell, J. Pérez-Ramírez and C. Copéret, *Nature*, 2025, **642**, 613–619.
26 W. d. A. Bezerra, J. L. S. Milani, C. H. d. J. Franco, F. T. Martins, Â. de Fátima, Á. F. A. da Mata and R. P. das Chagas, *Mol. Catal.*, 2022, **530**, 112632.
27 A. Chowdhury, S. Bhattacharjee, R. Chatterjee and A. Bhaumik, *J. CO_2 Util.*, 2022, **65**, 102236.
28 M. Pander, M. Janeta and W. Bury, *ACS Appl. Mater. Interfaces*, 2021, **13**, 8344–8352.
29 F. Hernandez, M. Yang, N. Nagelj, A. Y. Lee, H. Noh, K. P. Hur, X. Fu, C. J. Savoie, A. M. Schwartzberg and J. H. Olshansky, *Nanoscale*, 2024, **16**, 5624–5633.
30 S. Roy, B. Banerjee, A. Bhaumik and S. M. Islam, *RSC Adv.*, 2016, **6**, 31153–31160.
31 G. Li, X. Sui, X. Cai, W. Hu, X. Liu, M. Chen and Y. Zhu, *Angew. Chem., Int. Ed.*, 2021, **60**, 10573–10576.
32 S. Gratious, E. N. Nahan, R. Jin and S. Mandal, *Acc. Mater. Res.*, 2024, **5**, 1291–1302.
33 R. R. Shaikh, S. Pornpraprom and V. D'Elia, *ACS Catal.*, 2018, **8**, 419–450.
34 S. Bhattacharjee, S. Chongdar, A. Modak, P. Bhanja, B. K. Jena and A. Bhaumik, *Green Chem.*, 2022, **24**, 8853–8862.
35 B. Limburg, C. Maquilón and A. W. Kleij, in *CO_2 as a Building Block in Organic Synthesis*, 2020, pp. 1–28, DOI: 10.1002/9783527821952.ch1.
36 A. Balapure, J. Ray Dutta and R. Ganesan, *RSC Appl. Interfaces*, 2024, **1**, 43–69.
37 A. K. Patra, V. Amoli, A. K. Sinha and D. Kim, *ChemCatChem*, 2020, **12**, 2315–2323.
38 A. K. Patra, N. T. Vo and D. Kim, *Appl. Catal., A*, 2017, **538**, 148–156.
39 H. Li, Y. Zhou, W. Tu, J. Ye and Z. Zou, *Adv. Funct. Mater.*, 2015, **25**, 998–1013.
40 S. Sarkar, S. A. Ali, S. Sarkar, S. Banerjee, D. Kim and A. K. Patra, *ACS Appl. Nano Mater.*, 2025, **8**, 16398–16409.
41 S. A. Ali, S. Sarkar, S. Sarkar, S. Banerjee and A. K. Patra, *Surf. Interfaces*, 2025, **72**, 107061.
42 S. Sarkar, S. Banerjee, S. Sarkar, S. A. Ali and A. K. Patra, *J. Mol. Struct.*, 2025, **1348**, 143414.
43 R. Gogoi, P. Garg, P. P. Das, A. K. Rajak, N. Nath, S. Roy and K. Raidongia, *Nano Energy*, 2024, **131**, 110187.
44 X. Fu, J. Wang, D. Huang, S. Meng, Z. Zhang, L. Li, T. Miao and S. Chen, *ACS Catal.*, 2016, **6**, 957–968.
45 J. Hu, T. Ma, W. Shen, J. Wang, Z. Chen, L. Liang, Y. Zhang, J. Chen and Z. Li, *J. Alloys Compd.*, 2022, **920**, 165800.
46 L. Chen, K. Li, Y. Yang, T. Xue, H. Wang, B. Lei, J. Sheng, F. Dong and Y. Sun, *J. Hazard. Mater.*, 2023, **444**, 130436.
47 G. K. Dalapati, H. Sharma, A. Guchhait, N. Chakrabarty, P. Bamola, Q. Liu, G. Saianand, A. M. Sai Krishna, S. Mukhopadhyay, A. Dey, T. K. S. Wong, S. Zhuk, S. Ghosh, S. Chakrabortty, C. Mahata, S. Biring, A. Kumar, C. S. Ribeiro, S. Ramakrishna, A. K. Chakraborty, S. Krishnamurthy, P. Sonar and M. Sharma, *J. Mater. Chem. A*, 2021, **9**, 16621–16684.
48 P. Bhanja, B. Mohanty, A. K. Patra, S. Ghosh, B. K. Jena and A. Bhaumik, *ChemCatChem*, 2019, **11**, 583–592.
49 L. Du, K. Gu, M. Zhu, J. Zhang and M. Zhang, *Sens. Actuators, B*, 2019, **288**, 298–306.

50 S. Sarkar, S. Sarkar and A. K. Patra, *ChemNanoMat*, 2022, **8**, e202200294.
51 S. Banerjee, S. Sarkar, S. Sarkar and A. K. Patra, *Inorg. Chem. Commun.*, 2024, **160**, 111925.
52 S. Paul, S. Basak and W. Ali, *ACS Omega*, 2019, **4**, 21827–21838.
53 X. Lian, Z. Chen, X. Yu, T. Fan, Y. Dong, H. Zhai, W. Fang and X. Yi, *Nanoscale*, 2019, **11**, 9444–9456.
54 L. Mohapatra, M. Nagaraju, S. Suman and A. K. Kushwaha, *J. Alloys Compd.*, 2022, **928**, 167127.
55 W. Marynowski, M. Saski, B. Pałuba, M. Pisarek and J. Lewiński, *ACS Appl. Electron. Mater.*, 2022, **4**, 2253–2263.
56 L. Dai, C. Strelow, T. Kipp, A. Mews, I. Benkenstein, D. Eifler, T. H. Vuong, J. Rabeah, J. McGettrick, R. Lesyuk and C. Klinke, *Chem. Mater.*, 2021, **33**, 275–284.
57 B. Chen, Y. Duan, J. Tan, Y. Li, S. Li and D. Zhang, *Adv. Funct. Mater.*, 2025, **35**(19), 2425956.
58 L. Lu, Y. Cheng, Z. Liang, S. Yan, G. Qiao and Z. Zou, *Inorg. Chem.*, 2023, **62**, 2934–2941.
59 Y. Li, B. Chen, P. Ouyang, Y. Duan, W.-J. Ong and F. Dong, *Chem. Eng. J.*, 2023, **451**, 138695.
60 S. A. Ali, S. Sarkar and A. K. Patra, *ACS Appl. Mater. Interfaces*, 2024, **16**, 38061–38072.
61 Q. Yang, H. Peng, Q. Zhang, X. Qian, X. Chen, X. Tang, S. Dai, J. Zhao, K. Jiang, Q. Yang, J. Sun, L. Zhang, N. Zhang, H. Gao, Z. Lu and L. Chen, *Adv. Mater.*, 2021, **33**, 2103186.
62 Y. Wu, X. Song, S. Xu, Y. Chen, O. Oderinde, L. Gao, R. Wei and G. Xiao, *Dalton Trans.*, 2020, **49**, 312–321.
63 K. Wu, T. Su, D. Hao, W. Liao, Y. Zhao, W. Ren, C. Deng and H. Lü, *Chem. Commun.*, 2018, **54**, 9579–9582.
64 C. Liu, H. Niu, D. Wang, C. Gao, A. Said, Y. Liu, G. Wang, C.-H. Tung and Y. Wang, *ACS Catal.*, 2022, **12**, 8202–8213.
65 H. Liu, J. Xia, N. Zhang, H. Cheng, W. Bi, X. Zu, W. Chu, H. Wu, C. Wu and Y. Xie, *Nat. Catal.*, 2021, **4**, 202–211.
66 H. Liu, H. Wang, Q. Song, K. Küster, U. Starke, P. A. van Aken and E. Klemm, *Angew. Chem., Int. Ed.*, 2022, **61**, e202117058.
67 W. Zhang, Y. Yan, J. Wang, Z. Yang, T. Li, H. Li, S. Yan, T. Yu, W. Fan and Z. Zou, *Dalton Trans.*, 2023, **52**, 7129–7135.
68 Y. Wang, H. Liu, Q. Shi, Z. Miao, H. Duan, Y. Wang, H. Rong and J. Zhang, *Angew. Chem., Int. Ed.*, 2024, **63**, e202404911.
69 Q. Li, H. Yang, M. Li, K. Zhao, B. Duan, C. Zhang, H. Wang, C. Qiao, H. Chang and T. Lin, *Ind. Eng. Chem. Res.*, 2020, **59**, 8136–8144.
70 W. Natongchai, S. Posada-Pérez, C. Phungpanya, J. A. Luque-Urrutia, M. Solà, V. D'Elia and A. Poater, *J. Org. Chem.*, 2022, **87**, 2873–2886.